Supplement of Earth Syst. Sci. Data, 18, 5167–5186, 2026
https://doi.org/10.5194/essd-18-5167-2026-supplement

Supplement of

A combination of time-variable gravity field solutions from multi-satellite datasets (1993–2024) via constrained collocation model

Lin Zhang et al.

Correspondence to: Yunzhong Shen (yzshen@tongji.edu.cn)

S1. Supplementary Tables and Figures

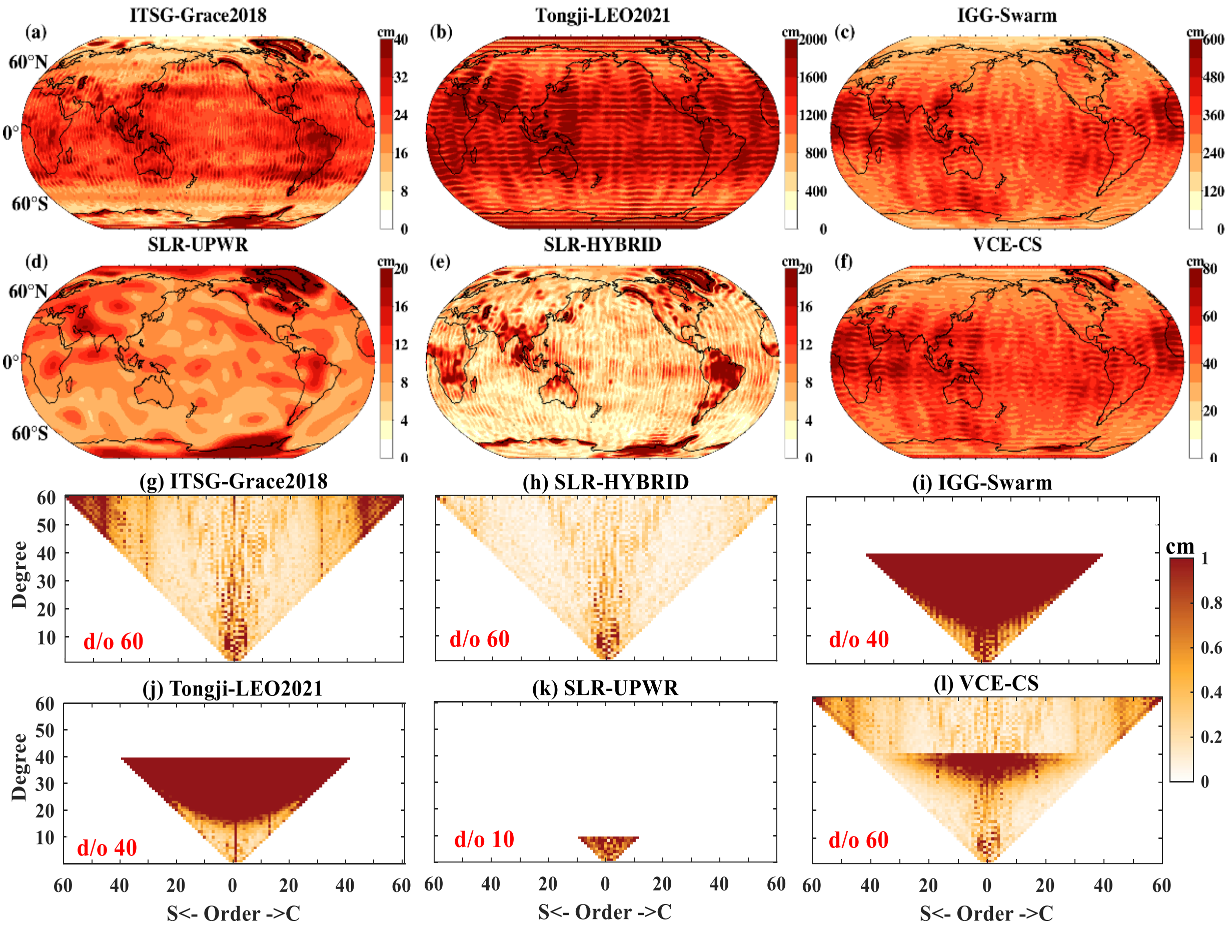

Figure S1: (a-f) RMS of spatial TWSAs and (g-l) SHCs derived from individual and VCE-CS.

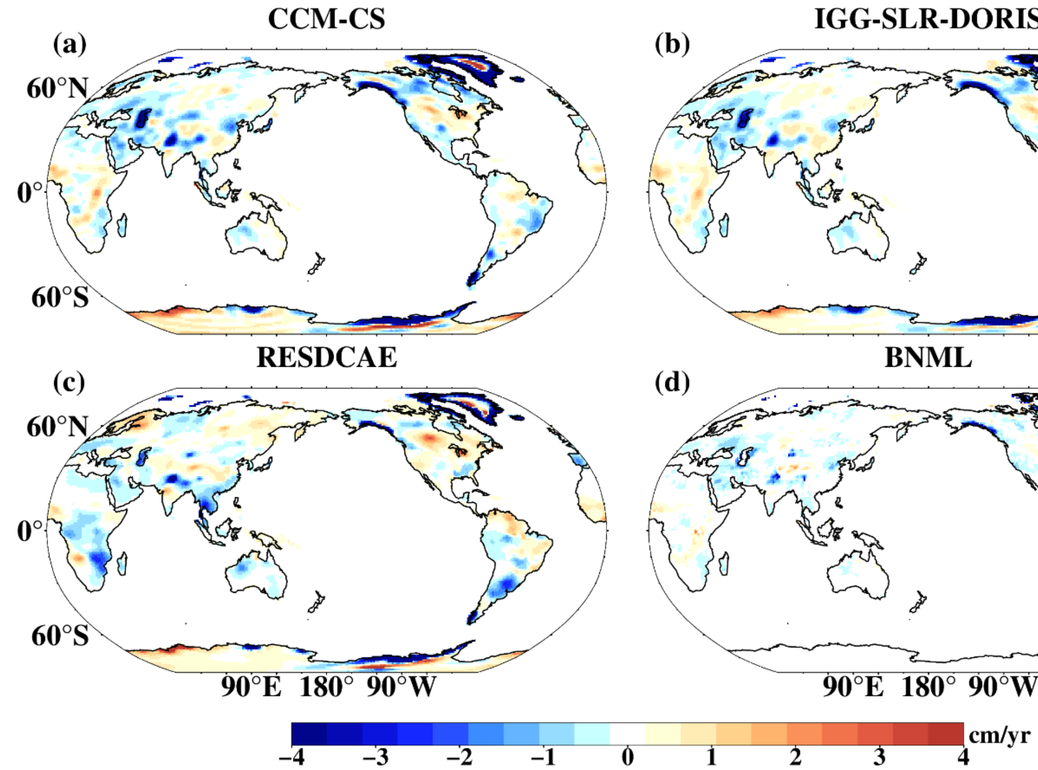

Figure S2: Linear trends of global TWSA during the common period from January 1994 to December 2020.

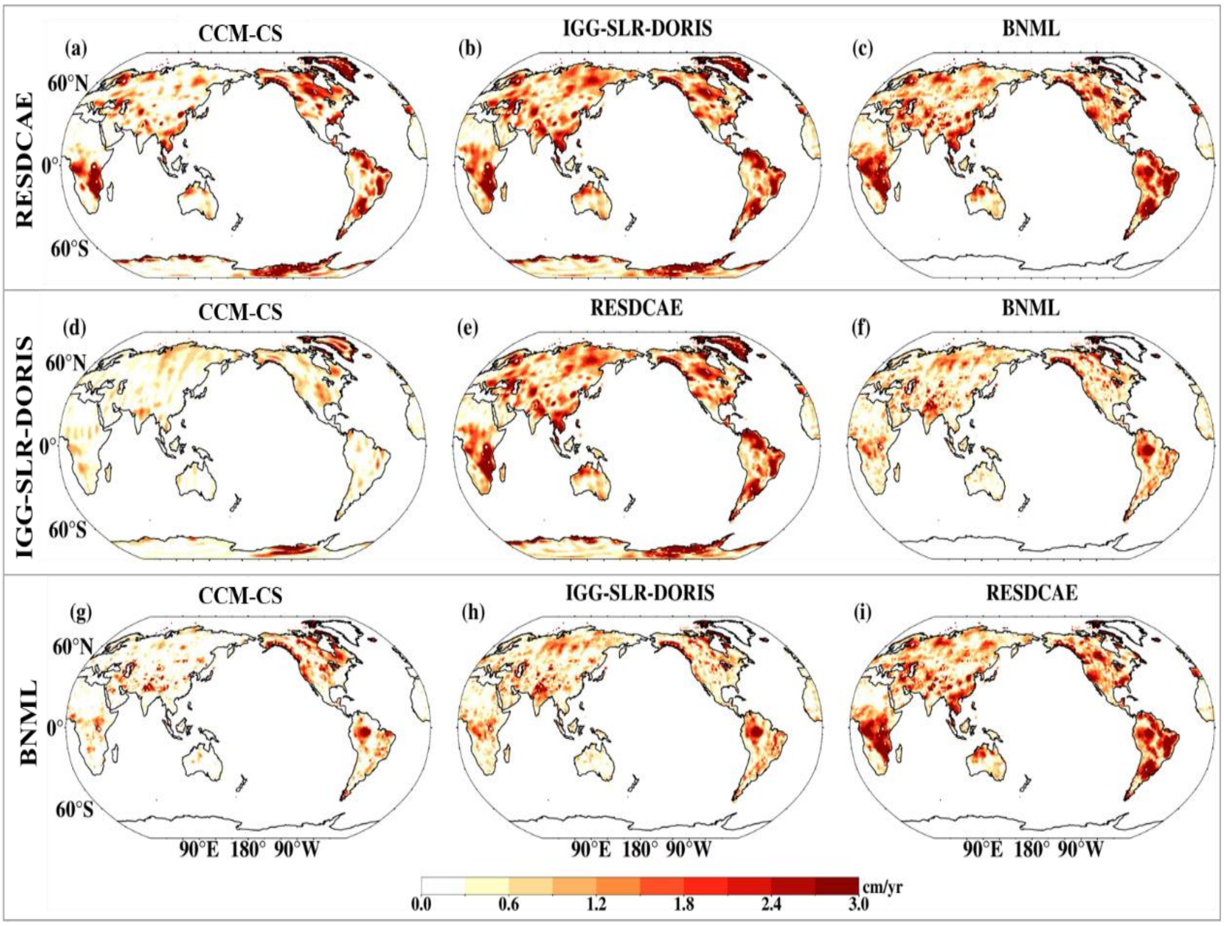

Figure S3: Absolute differences in linear trend of global TWSA from various solutions relative to RESDCAE, IGG-SLR-DORIS, and BNML corresponding to the first to third rows (January 1994 to December 2020).

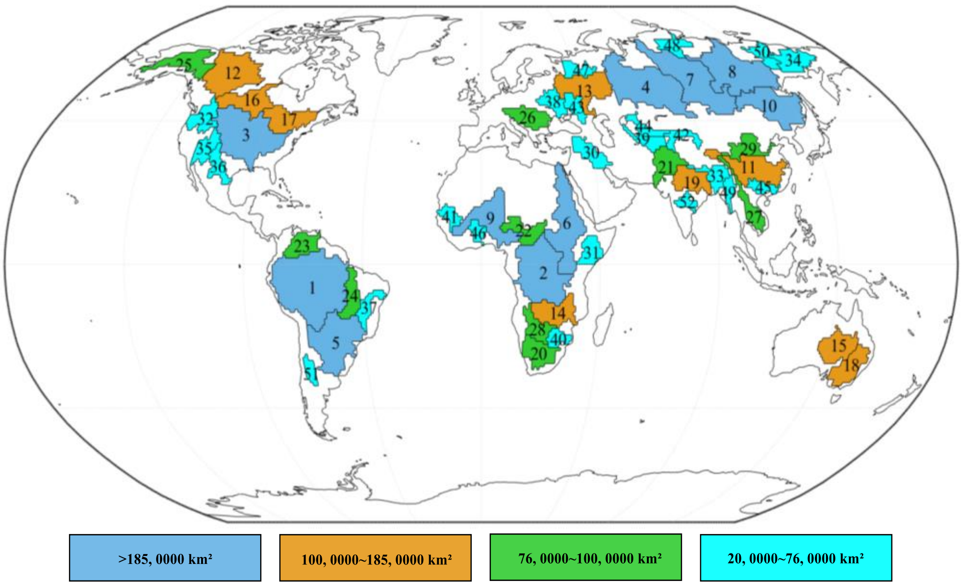

1. Amazon	2. Congo	3. Mississippi	4. Ob	5. Parana	6. Nile	7. Yenisey	8. Lena	9. Niger
10. Amur	11. Yangtze	12. Mackenzie	13. Volga	14. Zambeze	15. Lake_Eyre	16. Nelson	17. St_Lawrence	18. Murray
19. Ganges	20. Orange	21. Indus	23. Orinoco	24. Tocantins	25. Yukon	26. Danube	27. Mekong	28. Cubango
29. Yellow	30. Euphrates	31. Jubba	32. Columbia	34. Kolyma	35. Colorado	36. Rio_Grande	37.Sao_Francisco	38. Dniepr
39. Amu_Darya	40. Limpopo	41. Senegal	42. Tarim	43. Don	44. Syr_Darya	45. Xi_Hsi_Pearl	46. Volta	47. Northern
48. Khatanga	49. Irrawaddy	50. Indigirka	51. Salado	52. Godavari				

Figure S4: Spatial distributions of 52 major basins over the world, with different colors representing various area scales.

Table S1. Details of multi-type data products.

Data type		Sources	Period	Maximum d/o (Grid resolutions)
TVGFS	GRACE/GFO	ITSG-Grace2018 [1]	2002.04-2024.12	60
	Swarm	IGG-Swarm [2]	2014.08-2021.03	40
	LEO	Tongji-LEO2021 [3]	1993.01-2004.12	
	SLR	IGG-SLR-UPWR [4]	1995.02-2023.11	10
		IGG-SLR-HYBRID [5]	1993.01-2020.12	60
Previous studies	IGG-SLR-DORIS [6]	GRACE SHCs/SLR/DORIS	1984.01-2023.12	60
	BNML [7]	NOAH/CLSM	1960.01-2022.12	1° x 1°
	RESDCAE [8]	GRACE Mascon/SLR/ERA5	1994.01-2021.12	
Mascon		CSR RL06 [9]	2002.04-2024.12	0.25 ° x 0.25 °
		JPL RL06 [10]		3° x 3 °
Sea level budget	$\Delta h_{\text{thermosteric}}$	[11]	1900.01-2018.12	Time series (Yearly)
	Δh_{GrIS}, Δh_{AIS}			
	GMSL	[11]		
		Satellite altimetry [12]	1993.01-2024.12	Time series (Monthly)
Water balance equation	Precipitation	CRUv4.09 [13]	1901.01-2024.12	0.5 ° x 0.5 °
		GPCCv2020 [14]	1982.01-2020.12	1 ° x 1 °
		TRMM [15]	1998.01-2020.01	0.25 ° x 0.25 °
	Evaporation	GLEAM [16]	1993.01-2024.12	0.1 ° x 0.1 °
		FluxCom [17]	2001.01-2013.12	0.5 ° x 0.5 °
		PML-v2 [18]	2002.06-2019.08	0.5 ° x 0.5 °
		Global-ET [19]	1993.01-2006.12	1 ° x 1 °
	Runoff	G-RUN [20]	1901.07-2019.12	0.5 ° x 0.5 °
		SURFEX-TRIP [21]	1979.01-2012.12	
		W3RA [22]		
		CNRDv1 [23]	2001.01-2018.12	0.25 ° x 0.25 °
		GRDC[24]	1950.01–2023.12	In-situ
Ice Sheets	AIS, GrIS	IMBIE [25]	1993.01-2020.12	Time series (Monthly)

Table S2. Notation box for core symbols used in the Methodology.

Symbol	Description	Dimension	Initial appears in
k, i	Month index and TVGFS index.	Scalars	Eq. (1)
l, m	Spherical harmonic degree and order.	Scalars	Eq. (1)
$M_{k,i}$	Number of SHCs provided by the i-th TVGFS at month k.	1×1	Eq. (3)
M	Number of SHCs in the target combined TVGFS.	1×1	Eq. (3)
q_k	Number of individual TVGFS available at month k.	1×1	Eq. (2)
N_k	Total number of observations at month k	1×1	Eq. (2)
G	Number of global grids for one month	G×1	Eq. (7)
$y_{k,i}^{lm}$	SHC from the i-th TVGFS for degree l and order m at month k.	1×1	Eq. (1)
Δt_k	Time interval between month k and the reference epoch.	1×1	Eq. (1)
$a_{0,i}^{lm}, \ldots, a_{6,i}^{lm}$	Deterministic coefficients: constant, trend, acceleration, annual and semi-annual.	1×1	Eq. (1)
$s_{k,i}^{lm}$	Non-seasonal signal (NSS) for the corresponding SHC.	1×1	Eq. (1)
$e_{k,i}^{lm}$	Observation error corresponding to $y_{k,i}^{lm}$.	1×1	Eq. (1)
$\boldsymbol{y}_{k,i}$	Observation vector stacking SHCs from the i-th TVGFS at month k.	$M_{k,i}$×1	Eq. (2)
$\boldsymbol{y}_k$	Combined observation vector stacking all available TVGFS at month k.	N_k×1	Eq. (2)
$\boldsymbol{A}_{k,i}$	Design matrix for the i-th TVGFS harmonic model.	$M_{k,i}$ ×7M	Eq. (4)
$\boldsymbol{A}_k$	Stacked design matrix for all available TVGFS at month k.	N_k×7M	Eq. (2)
$\boldsymbol{B}_{k,i}$	Selection/extension matrix mapping target SHCs to the i-th TVGFS support.	$M_{k,i}$ × M	Eq. (3)
$\boldsymbol{B}_k$	Stacked selection matrix for all available TVGFS at month k.	N_k× M	Eq. (2)
$\boldsymbol{x}$	Combined deterministic parameter vector for all target SHCs.	7M×1	Eq. (2)
$\boldsymbol{s}_k$	Combined NSS vector at month k.	M×1	Eq. (2)
$\boldsymbol{e}_k$	Combined observation-error vector at month k.	N_k× 1	Eq. (2)
$\boldsymbol{P}_{e_k}$	Block-diagonal weight matrix of combined observation errors.	N_k×N_k	Eq. (2)
$\boldsymbol{\Sigma}_{e_k}$	Covariance matrix of combined observation errors.	N_k×N_k	Eq. (2)
$\sigma_{e_i}^2$	Time-invariant variance factor for the i-th TVGFS.	1×1	Eq. (2)
$\boldsymbol{\Phi}_{k,j}$	State transition matrix from epoch j to k in the GM model.	M×M	Eq. (5)
r	Order of multi-order GM model	1×1	Eq. (5)
τ_s	Correlation time of the GM process.	1×1	Eq. (6)
σ_s^2	Variance component of the GM process.	1×1	Eq. (6)
$\boldsymbol{w}_k$	GM process noise at month k.	M×1	Eq. (5)
$\boldsymbol{Q}_k$	Covariance matrix of GM process noise.	M×M	Eq. (6)
$\boldsymbol{D}$	Diagonal degree-dependent scale matrix.	M×M	Eq. (6)
$\bar{\boldsymbol{s}}_k$	Predicted NSS before the Kalman update.	M×1	Eq. (9)
$\boldsymbol{\Sigma}_{\bar{s}_k}$	Predicted/updated covariance matrix of NSS at month k.	M×M	Eq. (9)
α	Regularization parameter selected by the minimum-MSE criterion.	1×1	Eq. (7)
$\boldsymbol{R}$	Regularization matrix propagated from the spatial expression of $\boldsymbol{x}$.	7M×7M	Eq. (7)
$\boldsymbol{T}$	Spherical harmonic analysis matrix used in constructing $\boldsymbol{R}$	7M×7G	Eq. (7)
$\boldsymbol{x}_g$	Spatial expression of the deterministic parameter vector $\boldsymbol{x}$.	7G×1	Eq. (7)
$\boldsymbol{K}_k$	Kalman gain matrix for updating NSS at month k.	M×N_k	Eq. (11)
L	Cost function minimized to determine r, τ_s, and σ_s^2.	1×1	Eq. (12)
$\bar{\boldsymbol{v}}_k$	Prediction residual used in the GM-model cost function.	N_k ×1	Eq. (12)
$\boldsymbol{C}_k$	Covariance matrix of $\bar{\boldsymbol{v}}_k$.	N_k×N_k	Eq. (12)
$\boldsymbol{M}_{\hat{x}}$	MSE matrix of the combined deterministic parameter vector $\hat{\boldsymbol{x}}$.	7M×7M	Eq. (12)

S2. Iterative process for combining TVGFS

Since the estimated equations for $\widehat{\boldsymbol{x}}$ and $\widehat{\boldsymbol{s}}_k$ in Eqs. (8) and (11) are mutually nested; the estimation process is iteratively conducted. This process involves updating the variance factors $\sigma_{e_i}^2$, regularization parameter α, regularization matrix $\boldsymbol{R}$, optimal variables of GM model, as summarized in Fig. S5.

The iteration initializes with variance factors $\left(\sigma_{e_i}^2\right)^{(0)} = 1$ for $i = 1, \dots, q_k$, NSS $(\widehat{\boldsymbol{s}}_k)^{(0)} = \boldsymbol{0}$, and parameters obtained from least-squares solutions ($(\widehat{\boldsymbol{x}})^{(0)} = \widehat{\boldsymbol{x}}_{ls}$). At hth iteration, covariance matrix $\boldsymbol{\Sigma}_{e_k}^{(h)} = \left(\sigma_{e_{k,i}}^2\right)^{(h)} \boldsymbol{P}_{e_{k,i}}^{-1}$ and regularization matrix $\boldsymbol{R}^{(h)} = \left(\boldsymbol{D}\boldsymbol{T}\widehat{\boldsymbol{x}}_g^{(h)}\left(\widehat{\boldsymbol{x}}_g^{(h)}\right)^T \boldsymbol{T}^T \boldsymbol{D}^T\right)^{-1}$ are computed beforehand, where $\widehat{\boldsymbol{x}}_g^{(h)}$ represents the spatial expression of $(\widehat{\boldsymbol{x}})^{(h)}$. $\alpha^{(h)}$ is determined using the minimum MSE criterion [26; 27]. Subsequently, $(\widehat{\boldsymbol{x}})^{(h+1)}$ is updated via Eq. (8), while $(\widehat{\boldsymbol{s}}_k)^{(h+1)}$ is updated using bi-directional KF (Eqs. (10) and (11)) with the GM variables r, τ_s, and σ_s^2 selected by minimizing Eq. (12) over predefined grid-search ranges: r =1-6, τ_s =30-360 days with a 30-day interval, and σ_s^2=0.001-10 cm^2 with an interval of 0.01 cm^2. Finally, the variance factors $\left(\sigma_{e_{k,i}}^2\right)^{(h+1)}$ are updated using bias-corrected VCE [28] with $\alpha^{(h)}$, $\boldsymbol{R}^{(h)}$, and $(\widehat{\boldsymbol{x}})^{(h+1)}$.

Finally, the iteration continues until the differences of regularization solutions $\widehat{\boldsymbol{x}}$ between consecutive iterations falls below 1% (i.e., $\frac{\|\widehat{x}^{(h)} - \widehat{x}^{(h-1)}\|_2}{\|\widehat{x}^{(h-1)}\|_2} < 0.01$). The combined TVGFS $\widehat{\boldsymbol{y}}_k = \overline{\boldsymbol{A}}_k \widehat{\boldsymbol{x}} + \widehat{\boldsymbol{s}}_k$, with $\overline{\boldsymbol{A}}_k = [1 \quad \Delta t_k \quad \Delta t_k^2 \quad \sin(2\pi\Delta t_k) \quad \cos(2\pi\Delta t_k) \quad \sin(4\pi\Delta t_k) \quad \cos(4\pi\Delta t_k)] \otimes \boldsymbol{I}_M$.

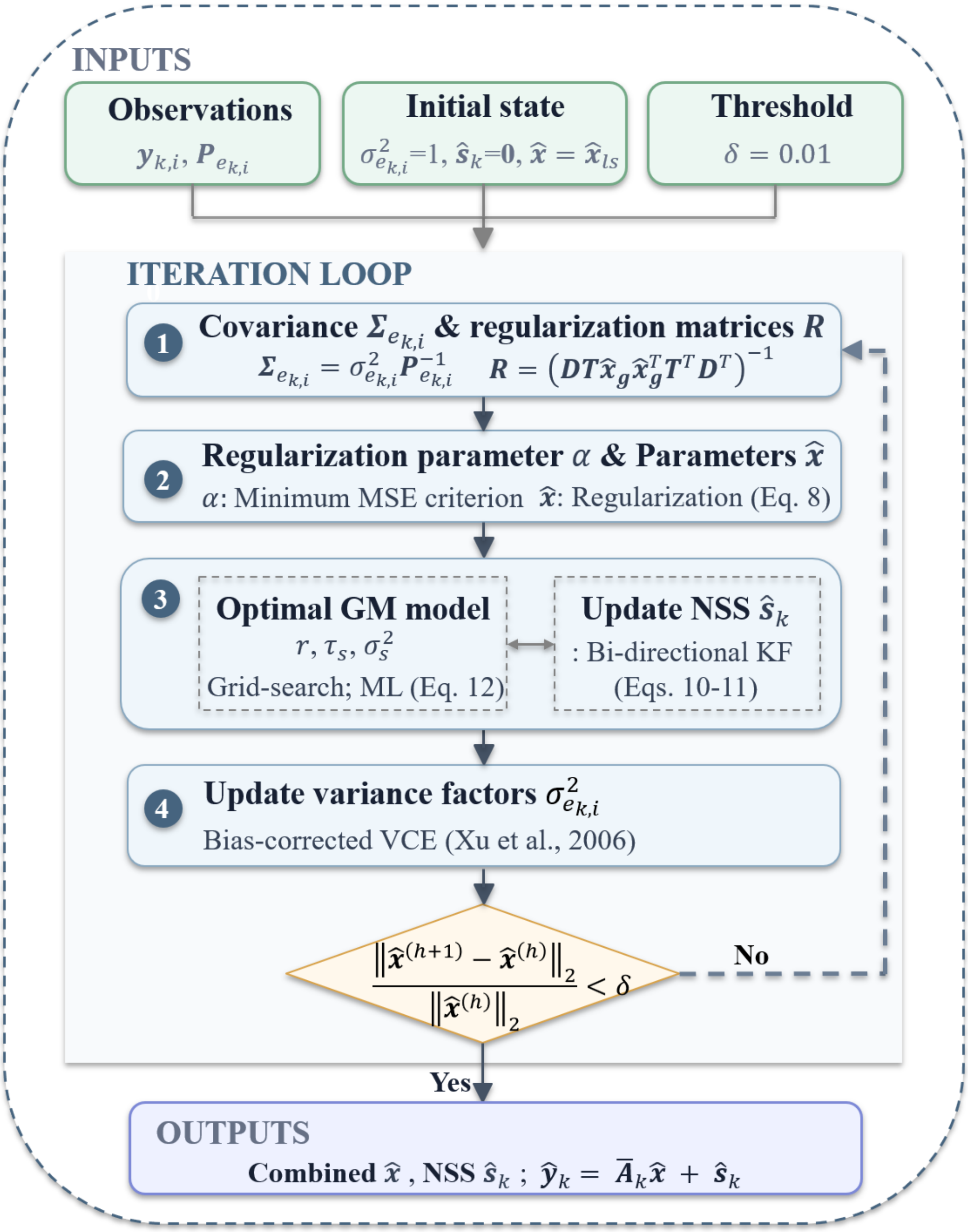

Figure S5: Flowchart for iteratively combining TVGFS (The symbols are introduced in Tab. S2).

S3. Fusion of in-situ observations with gridded simulated runoff

For month t, the observation equation is written as,

$$\boldsymbol{y}_t = \boldsymbol{H}_t\boldsymbol{x}_t + \boldsymbol{\varepsilon}_t \tag{S1}$$

where $\boldsymbol{y}_t$ is the observation vector formed from monthly GRDC runoff observations in terms of runoff depth, $\boldsymbol{\varepsilon}_t$ is the observation error, $\boldsymbol{x}_t$ is the simulated runoff state vector, $\boldsymbol{H}_t$ is the design matrix that maps gridded runoff to each in-situ station by aggregating grid-cell runoff over the corresponding station-controlled drainage area [29].

The fused runoff state is obtained by minimizing the cost function,

$$J(\boldsymbol{x}_t) = (\boldsymbol{x}_t - \boldsymbol{x}_t^b)^T(\boldsymbol{Q}_t^b)^{-1}(\boldsymbol{x}_t - \boldsymbol{x}_t^b) + (\boldsymbol{y}_t - \boldsymbol{H}_t\boldsymbol{x}_t)^T\boldsymbol{\Sigma}_t^{-1}(\boldsymbol{y}_t - \boldsymbol{H}_t\boldsymbol{x}_t) \tag{S2}$$

where the background state $\boldsymbol{x}_t^b = \frac{1}{N}\sum_{k=1}^{N}\boldsymbol{x}_t^{b,(k)}$ with $\boldsymbol{x}_t^{b,(k)}$ denoting the kth simulated runoff product among N ensemble members; the background error covariance $\boldsymbol{Q}_t^b = \frac{1}{N-1}\sum_{k=1}^{N}\left(\boldsymbol{x}_t^{b,(k)} - \mathbf{x}_t^b\right)\left(\boldsymbol{x}_t^{b,(k)} - \mathbf{x}_t^b\right)^T$; and the observation-error covariance $\boldsymbol{\Sigma}_t = \mathrm{diag}\left(\sigma_{1,t}^2, \ldots, \sigma_{m_t,t}^2\right)$, with $\sigma_{s,t}$ representing the uncertainty of the runoff observation at sth station, and m_t is the number of valid GRDC stations at month t.

The corresponding ensemble solution $\boldsymbol{x}_t^a$ is,

$$\boldsymbol{x}_t^a = \boldsymbol{x}_t^b + \boldsymbol{K}_t(\boldsymbol{y}_t - \boldsymbol{H}_t\boldsymbol{x}_t^b) \tag{S3}$$

where $\boldsymbol{K}_t = \boldsymbol{Q}_t^b\boldsymbol{H}_t^T(\boldsymbol{H}_t\boldsymbol{Q}_t^b\boldsymbol{H}_t^T + \boldsymbol{\Sigma}_t)^{-1}$ is the gain matrix.

S4. Evaluation Metrics

(1) Sea level budget

TWS contribution to global mean sea level (Δh_{GMSL}) variations is deived by subtracting thermosteric expansion ($\Delta h_{\mathrm{therm}}$) and mass changes of Greenland (Δh_{GrIS}) and Antarctic (Δh_{AIS}) Ice Sheets from total GMSL [11],

$$\Delta h_{\mathrm{TWS}} = \Delta h_{\mathrm{GMSL}} - \Delta h_{\mathrm{therm}} - \Delta h_{\mathrm{GrIS}} - \Delta h_{\mathrm{AIS}} \tag{S4}$$

(2) Water balance equation

TWSCs from TVGFS ($\Delta\mathrm{TWSC}_{\mathrm{TVGFS}}$) computed from TWSAs between two adjacent months can be evaluated by computing the misclosure with water balance estimates composed of precipitation (P), runoff (R), and evaporation (E) [30],

$$\Delta\mathrm{TWSC}_{\mathrm{TVGFS}} = \mathrm{P} - \mathrm{R} - \mathrm{E} \tag{S5}$$

(3) Land-to-ocean Signal-to-Noise Ratios (SNRs)

The SNR at latitude θ_i (i.e., SNR_{θ_i}) is computed using the Root Mean Square (RMS) of mass changes over land ($\mathrm{MASS}_{\mathrm{land},\theta_i}$) and ocean ($\mathrm{MASS}_{\mathrm{ocean},\theta_i}$) at the corresponding latitude[31; 32],

$$\mathrm{SNR}_{\theta_i} = \frac{\mathrm{RMS}\left(\mathrm{MASS}_{\mathrm{land},\theta_i} + \mathrm{Err}_{\theta_i}\right)}{\mathrm{RMS}\left(\mathrm{MASS}_{\mathrm{ocean},\theta_i} + \mathrm{Err}_{\theta_i}\right)} \tag{S6}$$

The overall SNR is determined using the global latitude weighted average, $\mathrm{SNR} = \frac{\sum_{i=1}^{n}\cos\theta_i \cdot \mathrm{SNR}_{\theta_i}}{\sum_{i=1}^{n}\cos\theta_i}$; n indicates the number of latitude divisions in the global grid.

(4) Degree Power σ_l^2

$$\sigma_l^2 = \frac{\sum_{m=0}^{l}\left[\left(\Delta C_{lm}^{\gamma}\right)^2 + \left(\Delta S_{lm}^{\gamma}\right)^2\right]}{2l+1} \tag{S7}$$

where, C_{lm}^{γ} and ΔS_{lm}^{γ} are filtered SHCs at degree l and order m[33].

(5) Nash-Sutcliffe Efficiency (NSE)

$$\mathrm{NSE} = 1 - \frac{\sum_{t=1}^{n}(\mathrm{TWSA_{evaluated}}(t) - \mathrm{TWSA_{reference}}(t))^2}{\sum_{t=1}^{n}(\mathrm{TWSA_{evaluated}}(t) - \overline{\mathrm{TWSA_{reference}}})^2} \tag{S8}$$

where, TWSA derived from various solutions to be evaluated and the references are denoted as $\mathrm{TWSA_{filtered}}$ and $\mathrm{TWSA_{reference}}$; $\overline{\mathrm{TWSA_{reference}}}$ is the mean value of $\mathrm{TWSA_{reference}}$. NSE approaching 1 means excellent consistency while negative NSE denotes worse consistency[34].

References

[1] Kvas, A., Behzadpour, S., Ellmer, M., Klinger, B., Strasser, S., Zehentner, N., and Mayer-Gürr, T.: ITSG-Grace2018: Overview and Evaluation of a New GRACE-Only Gravity Field Time Series, Journal of Geophysical Research: Solid Earth, 124(8), 9332-9344, https://doi.org/10.1029/2019JB017415, 2019.

[2] Lück, C., Kusche, J., Rietbroek, R., and Löcher, A.: IGG-Swarm: Temporal Gravity Models from Swarm, GFZ Data Services [data set], https://doi.org/10.5880/icgem.2021.002, 2021.

[3] Chen, Q., Wang, F., Shen, Y., Zhang, X., Nie, Y., and Chen, J.: Monthly Gravity Field Solutions From Early LEO Satellites' Observations Contribute to Global Ocean Mass Change Estimates Over 1993~2004, Geophysical Research Letters, 49(21), e2022GL099917, https://doi.org/10.1029/2022GL099917, 2022.

[4] Gałdyn, F., Sośnica, K., Zajdel, R., Meyer, U., and Jäggi, A.: Long-term ice mass changes in Greenland and Antarctica derived from satellite laser ranging, Remote Sensing of Environment, 302, 113994, https://doi.org/10.1016/j.rse.2024.113994, 2024.

[5] Löcher, A., and Kusche, J.: A hybrid approach for recovering high-resolution temporal gravity fields from satellite laser ranging, Journal of Geodesy, 95, 6, https://doi.org/10.1007/s00190-020-01460-x, 2021.

[6] Löcher, A., Kusche, J., and Nie, Y.: A 40-year record of the Earth's time-variable gravity field from SLR and DORIS, Advances in Space Research, 76(3), 1281-1291, https://doi.org/10.1016/j.asr.2025.05.089, 2025.

[7] Mandal, N., Das, P., and Chanda, K.: Machine-learning-based reconstruction of long-term global terrestrial water storage anomalies from observed, satellite and land-surface model data, Earth System Science Data, 17(6), 2575-2604, https://doi.org/10.5194/essd-17-2575-2025, 2025.

[8] Uz, M., Akyılmaz, O., Shum, C. K., Atman, K. G., Olgun, S., and Güneş, Ö.: High-resolution temporal gravity field data products: Monthly mass grids and spherical harmonics from 1994 to 2021, Scientific Data, 11, 71, https://doi.org/10.1038/s41597-023-02887-5, 2024.

[9] Save, H., Bettadpur, S., and Tapley, B. D.: High-resolution CSR GRACE RL05 mascons, Journal of Geophysical Research: Solid Earth, 121(10), 7547-7569, https://doi.org/10.1002/2016JB013007, 2016.

[10] Watkins, M. M., Wiese, D. N., Yuan, D., Boening, C., and Landerer, F. W.: Improved methods for observing Earth's time variable mass distribution with GRACE using spherical cap mascons, Journal of Geophysical Research: Solid Earth, 120(4), 2648-2671, https://doi.org/10.1002/2014JB011547, 2015.

[11] Frederikse, T., Landerer, F., Caron, L., Adhikari, S., Parkes, D., Humphrey, V. W., Dangendorf, S., Hogarth, P., Zanna, L., Cheng, L., and Wu, Y. H.: The causes of sea-level rise since 1900, Nature, 584(7821), 393-397, https://doi.org/10.1038/s41586-020-2591-3, 2020.

[12] NASA-SSH: Global Mean Sea Level Trend from Integrated Multi-Mission Ocean Altimeters TOPEX/Poseidon, Jason-1, OSTM/Jason-2, Jason-3, and Sentinel-6 Version 5.2, NASA Physical Oceanography Distributed Active Archive Center [data set], https://doi.org/10.5067/GMSLM-TJ152, 2024.

[13] Harris, I., Osborn, T. J., Jones, P., and Lister, D.: Version 4 of the CRU TS monthly high-resolution gridded multivariate climate dataset, Scientific Data, 7, 109, https://doi.org/10.1038/s41597-020-0453-3, 2020.

[14] Schneider, U., Becker, A., Finger, P., Meyer-Christoffer, A., Rudolf, B., and Ziese, M.: GPCC Full Data Reanalysis Version 7.0 at 0.5°: Monthly Land-Surface Precipitation from Rain-Gauges Built on GTS-Based and Historic Data, Global Precipitation Climatology Centre at Deutscher Wetterdienst [data set], https://doi.org/10.5676/DWD_GPCC/FD_M_V7_050, 2015.

[15] Precipitation Processing System (PPS) at Goddard Space Flight Center: TRMM (TMPA/3B43) Rainfall Estimate L3 1 Month 0.25 Degree × 0.25 Degree V7, NASA Goddard Earth Sciences Data and Information Services Center [data set], https://doi.org/10.5067/TRMM/TMPA/MONTH/7, 2018.

[16] Miralles, D. G., Bonte, O., Koppa, A., Baez-Villanueva, O. M., Tronquo, E., Zhong, F., Beck, H. E., Hulsman, P., Dorigo, W., Verhoest, N. E. C., and Haghdoost, S.: GLEAM4: global land evaporation and soil moisture dataset at 0.1° resolution from 1980 to near present, Scientific Data, 12, 416, https://doi.org/10.1038/s41597-025-04610-y, 2025.

[17] Jung, M., Koirala, S., Weber, U., Ichii, K., Gans, F., Camps-Valls, G., Papale, D., Schwalm, C., Tramontana, G., and Reichstein, M.: The FLUXCOM ensemble of global land-atmosphere energy fluxes, Scientific Data, 6, 74, https://doi.org/10.1038/s41597-019-0076-8, 2019.

[18] Zhang, Y., Kong, D., Gan, R., Chiew, F. H., McVicar, T. R., Zhang, Q., and Yang, Y.: Coupled estimation of 500 m and 8-day resolution global evapotranspiration and gross primary production in 2002-2017, Remote Sensing of Environment, 222, 165-182, https://doi.org/10.1016/j.rse.2018.12.031, 2019.

[19] Zhang, K., Kimball, J. S., Nemani, R. R., and Running, S. W.: A continuous satellite-derived global record of land surface evapotranspiration from 1983 to 2006, Water Resources Research, 46(9), W09519, https://doi.org/10.1029/2009WR008800, 2010.

[20] Ghiggi, G., Humphrey, V., Seneviratne, S. I., and Gudmundsson, L.: G-RUN ENSEMBLE: A multi-forcing observation-based global runoff reanalysis, Water Resources Research, 57(5), e2020WR028787, https://doi.org/10.1029/2020WR028787, 2021.

[21] Decharme, B., Martin, E., and Faroux, S.: Reconciling soil thermal and hydrological lower boundary conditions in land surface models, Journal of Geophysical Research: Atmospheres, 118(14), 7819-7834, https://doi.org/10.1002/jgrd.50631, 2013.

[22] Van Dijk, A.: The Australian Water Resources Assessment System Technical Report 3: Landscape Model (Version 0.5) Technical Description, CSIRO [technical report], https://doi.org/10.4225/08/5852dd9bb578c, 2010.

[23] Gou, J., Miao, C., Samaniego, L., Xiao, M., Wu, J., and Guo, X.: CNRD v1.0: A high-quality natural runoff dataset for hydrological and climate studies in China, Bulletin of the American Meteorological Society, 102(5), E929-E947, https://doi.org/10.1175/BAMS-D-20-0094.1, 2021.

[24] Färber, C., Plessow, H., Mischel, S. A., Kratzert, F., Addor, N., Shalev, G., and Looser, U.: GRDC-Caravan: extending Caravan with data from the Global Runoff Data Centre, Earth System Science Data, 17(9), 4613-4625, https://doi.org/10.5194/essd-17-4613-2025, 2025.

[25] Shepherd, A., Ivins, E., Rignot, E., Smith, B., van den Broeke, M., Velicogna, I., Whitehouse, P., Briggs, K., Joughin, I., Krinner, G., Nowicki, S., Payne, A., Scambos, T., Schlegel, N., Geruo, A., Agosta, C., Ahlstrøm, A., Babonis, G., Barletta, V., Bjørk, A., Blazquez, A., Bonin, J., Colgan, W., Csatho, B., Cullather, R., Engdahl, M., Felikson, D., Fettweis, X., Forsberg, R., Gallee, H., Gardner, A., Gilbert, L., Gourmelen, N., Groh, A., Gunter, B., Hanna, E., Harig, C., Helm, V., Hogg, A., Horvath, A., Horwath, M., Khan, S., Kjeldsen, K., Konrad, H., Langen, P., Lecavalier, B., Loomis, B., Luthcke, S., McMillan, M., Melini, D., Mernild, S., Mohajerani, Y., Moore, P., Mottram, R., Mouginot, J., Moyano, G., Muir, A., Nagler, T., Nield, G., Nilsson, J., Noël, B., Otosaka, I., Pattle, M., Peltier, W., Pie, N., Rietbroek, R., Rott, H., Sørensen, L. S., Sasgen, I., Save, H., Scheuchl, B., Schrama, E., Schröder, L., Seo, K.-W., Simonsen, S., Slater, T., Spada, G.,

Sutterley, T., Talpe, M., Tarasov, L., van de Berg, W. J., van der Wal, W., van Wessem, M., Vishwakarma, B. D., Wagner, T., Wiese, D., Wilton, D., Wouters, B., and Wuite, J.: Antarctic and Greenland ice sheet mass balance 1992-2020 for IPCC AR6 (version 1.0), UK Polar Data Centre, Natural Environment Research Council, UK Research & Innovation [data set], https://doi.org/10.5285/77b64c55-7166-4a06-9def-2e400398e452, 2021.

[26] Shen, Y., Xu, P., and Li, B.: Bias-corrected regularized solution to inverse ill-posed models, Journal of Geodesy, 86(8), 597-608, https://doi.org/10.1007/s00190-012-0542-y, 2012.

[27] Ji, K., Shen, Y., Chen, Q., Li, B., and Wang, W.: An Adaptive Regularized Solution to Inverse Ill-Posed Models, IEEE Transactions on Geoscience and Remote Sensing, 60, 1-15, https://doi.org/10.1109/TGRS.2022.3205572, 2022.

[28] Xu, P., Shen, Y., Fukuda, Y., and Liu, Y.: Variance component estimation in linear inverse ill-posed models, Journal of Geodesy, 80(2), 69-81, https://doi.org/10.1007/s00190-006-0032-1, 2006.

[29] Clark, M. P., Rupp, D. E., Woods, R. A., Zheng, X., Ibbitt, R. P., Slater, A. G., Schmidt, J., and Uddstrom, M. J.: Hydrological data assimilation with the ensemble Kalman filter: Use of streamflow observations to update states in a distributed hydrological model, Advances in Water Resources, 31(10), 1309-1324, https://doi.org/10.1016/j.advwatres.2008.06.005, 2008.

[30] Zhang, L., Shen, Y., Chen, Q., and Wang, F.: Influence factors and mechanisms of 2015-2016 extreme flood in Pearl River Basin based on the WSDI from GRACE, Journal of Hydrology: Regional Studies, 47, 101376, https://doi.org/10.1016/j.ejrh.2023.101376, 2023.

[31] Chen, J. L., Wilson, C. R., Tapley, B. D., Save, H., and Crétaux, J.: Long-term and seasonal Caspian Sea level change from satellite gravity and altimeter measurements, Journal of Geophysical Research: Solid Earth, 122(3), 2274-2290, https://doi.org/10.1002/2016JB013595, 2017.

[32] Zhang, L., Shen, Y., Ji, K., and Chen, Q.: An Enhanced Parameter Filtering Approach for Postprocessing GRACE Monthly Gravity Field Models, IEEE Geoscience and Remote Sensing Letters, 22, 1-5, https://doi.org/10.1109/LGRS.2025.3575197, 2025.

[33] Kusche, J.: Approximate decorrelation and non-isotropic smoothing of time-variable GRACE-type gravity field models, Journal of Geodesy, 81(11), 733-749, https://doi.org/10.1007/s00190-007-0143-3, 2007.

[34] Nash, J. E., and Sutcliffe, J. V.: River flow forecasting through conceptual models Part I: A discussion of principles, Journal of Hydrology, 10(3), 282-290, https://doi.org/10.1016/0022-1694(70)90255-6, 1970.